J Porous Mater (2017) 24:1129–1138
DOI 10.1007/s10934-016-0352-3

Dual mesoporous carbon with high nitrogen doping level as an efficient electrode material for supercapacitors

Deyi Zhang[1,2] · Yubing Li[1] · Mei Han[1] · Kunjie Wang[1] · Liang Zhang[1] · Tiantian Yang[1] · Juanxia He[1]

Published online: 4 January 2017

Abstract This paper reports a dual mesoporous carbon (NDMC) with high nitrogen doping level derived from the amino production of the sucrose synthesized under hydrothermal condition. The S_{BET} and total pore volume of the reported materials reaches up to 1101 and 1.67 $cm^3\ g^{-1}$, the small mesopores center at about 3.22–3.31 nm while the larger mesopores locate at 8.98–12.58 nm. The doping content of the nitrogen heteroatoms is found to be more than 11.6 at.%, and depend on the carbonization temperature. The maximum specific capacitance of the reported materials reaches up to 512 F g^{-1} due to the additional contribution of pseudo-capacitance induced by the nitrogen heteroatoms doping. The capacitance retention rate is found to be up to 95% after 1000 times cycles. The dual mesoporous structure, high specific area, additional pseudo-capacitance, enhanced wettability and conductivity are found to response for the superior capacitance performance of the reported materials.

Keywords Dual mesoporous · High nitrogen doping level · Mesoporous carbon · Pseudo-capacitance

✉ Deyi Zhang
lzdeyizhang@163.com

[1] College of Petrochemical Technology, Lanzhou University of Technology, Lanzhou 730050, China

[2] Key Laboratory of Eco-Environment-Related Polymer Materials of Ministry of Education, Northwest Normal University, Lanzhou 730070, China

1 Instruction

In recent years, the intense research interest on advanced energy conversion and storage devices has been ignited once again due to the impressive prospects of electric vehicles. Lithium ion battery is the popular choice for electric vehicles due to their advantage of high energy density and relatively long cycle life. However, long charge time and lower power density are the fatal deficiency for electric vehicles using lithium ion battery as the power source. Supercapacitors, as an alternative choice, has been considered as a promising candidate solution to the mismatch between the fast growth in power required by devices and the inability of batteries to efficiently discharge at high rates due to the fast charge/discharge processes, high power density, and excellent cycle stability [1, 2]. Nevertheless, the energy stored in supercapacitors is currently an order of magnitude lower than batteries, which limits their adoption to those applications that require high cycle life and power density [3, 4]. Improvements in the energy density may enable numerous industrial and consumer applications for supercapacitors [1].

The capacitance performance of the electrode materials used for supercapacitors mainly depends on the specific surface area, pore architecture, surface physical and chemical activity, and conductivity. Various carbon materials, such as graphene [5], carbon nanotubes [6], carbon sphere [7], ordered mesoporous carbons [8], activated carbons [9], and their composites [2], have been explored as electrode materials for supercapacitors due to high specific surface area, good conductivity, and outstanding chemical inertness. Carbon-based supercapacitors store energy mainly by electrical double-layer capacitance (EDLC) mechanism. These type supercapacitors exhibit excellent power density, fast charge/discharge processes,

as well as long cycle life, however, the energy density is far lower than that of batteries. The supercapacitors based on the pseudo-capacitance electrode materials, such as RuO_2 [10] or MnO_2 [11], and electronically conducting polymers [12], or their composites [13, 14], store energy by reversible redox or faradaic charge-transfer reactions display high energy density, however, the low conductivity, poor compatibility with organic or acid electrolytes, and short cycle life have limited its practical application [11–14]. Although the hybrid electrode materials of carbon/pseudo-capacitance materials seems providing a potential solution for the mismatch between the high power density and energy density, the inherent defects of pseudo-capacitance materials cannot be entirely avoided. Meanwhile, the block effect the pseudo-capacitance materials particles on the pores of the carbon matrix would cause great decrease of the specific surface area, and then destroy the excellent EDLC performance of the porous carbon materials. So, exploring a new strategy for effectively combining the EDLC and pseudo-capacitance is an important challenge for the development of the high-performance supercapacitors.

Recently, the faradaic pseudo-capacitance generated on the surface of nitrogen-doped mesoporous carbon materials was revealed and its potentials application in the high performance supercapacitor has attracted extensive interesting [8, 15]. For instance, Lin et al. reported a nitrogen-doped few-layer mesoporous carbon with an extra high specific capacitance of 855 F g^{-1} due to the contribution of the faradaic pseudo-capacitance generated at nitrogen-associated defects [15]. However, most of these nitrogen doped mesoporous carbons are with monotonous mesopore structure, which impairs the transfer or diffusion of electrolyte ions in large resistance in mass transfer [16]. Dual mesopores carbons may provide a solution to this mass transfer problem, and have been successfully used as electrochemical materials [16].

Owing to low glycosidation temperature, sucrose is an ideal precursor for fabricating porous carbon electrode materials. Herein, we demonstrate a successful fabrication of dual mesoporous carbon with high nitrogen doping level using an amino group functional sucrose synthesized under hydrothermal condition as precursor. As far as our knowledge, using sucrose as initial precursor to fabricate nitrogen doped porous carbon has not yet reported. The fabricated NDMC materials exhibits dual mesoporoe structure, excellent textural properties, high nitrogen doping level and superior capacitance performance with a specific capacitance of up to 512 F g^{-1}. The enhanced electrolyte ions diffusion rate induced by dual mesoporoe structure, improved wettability and conductivity, and additional pseudo-capacitance were found to response for the superior capacitance performance of the reported materials.

2 Experiment

2.1 Synthesis of the precursor

The nitrogen-rich precursor was prepared via hydrothermal method by amination reaction between the sucrose and ammonia-water. In brief, 5.0 g of sucrose was dissolved in 50 mL of 30 wt% ammonia–water, and then the mixture solution was heated at 200 °C for 24 h by sealing in a 100 mL Teflon-lined stainless steel autoclave. The obtained brown solution was dried in a vacuum oven at 105 °C for 24 h. After that, the dried product was ground into fine powder and used as a nitrogen-rich precursor.

2.2 Fabrication of the NDMC materials

A nanocasting strategy was adopted to synthesize the NDMC materials using mesoporous SBA-15 molecular sieve as the template. In brief, dissolving 1.0 g of above precursor in 1.0 mL of alcohol, and then 0.1 mL of 98 wt% H_2SO_4 was added. Thus mixture solution was slowly dropped onto the surface of 1.0 g of the SBA-15 template. Then, the superfluous solvent was removed by heating at 80 °C for 2 h under vacuum, and pre-carbonizing which dried sample at 160 °C for 8 h. Then completely carbonizing the resultant brown product at 650–950 °C for 2 h under an argon atmosphere. After removing the silica template by HF (10 wt%) aqueous solution in atmosphere and repeated washing by distilled water and alcohol, a series of NDMC samples were fabricated. The got NDMC series samples synthesized at different carbonization temperatures are referred to as NDMC-x, where x denotes the carbonization temperature. The ordered mesoporous carbon CMK-3 using sucrose as precursor synthesized by the similar method were used as a non-doped sample to compare the textural and capacitance performance with the fabricated NDMC electrode materials.

2.3 Material characterization

The elements composition and chemical bond configuration of the precursor and fabricated NDMC samples were detected by CHNS element analyzer (Vario EL Cube) and X-ray photoelectron spectroscopy (XPS) performed on a Thermo Multilab 2000. The Fourier transform infrared spectroscopy (FTIR) measurements were conducted on a Nicolet Nexus 670 spectrometer in transmission mode using KBr pellets. Nitrogen adsorption/desorption isotherms were measured at 77 K with a Micromeritics ASAP 2020 volumetric adsorption analyzer. The specific surface areas, S_{BET} was determined from the linear part of the Brunauer, Emmett and Teller (BET) equation while the pore volume was calculated using the BET plot from the

amount of nitrogen gas adsorbed at the last adsorption point ($P/P_0 = 0.95$), and the pore size distribution was evaluated using the Barrett–Joyner–Halenda (BJH) method. A X'Pert X-ray defractometer (Phillips) with Cu K*a* radiation were used to collect the small-angle X-ray scattering (SAXS) of samples. The SEM images were conducted on a Hitachi S-4800 field emission scanning electron microscope and the transmission electron microscopy (TEM) experiments were obtained using a JEM-2010 microscope.

2.4 Electrochemical measures

All electrochemical experiments were performed on CHI 660E electrochemical workstation using a three-electrode system in 2 M KOH electrolyte solution. The fabricated NDMC samples were used as the working electrode, and a platinum slice and saturated calomel electrode (SCE) were used as the counter and reference electrode, respectively. The working electrode was prepared by mixing a certain sample of the fabricated materials (ca. 5 mg), acetylene black and polytetrafluoroethylene (PTFE) with a weight ratio of 85: 10: 5, and then coating the above mixture slurry on foamed Ni grids (10 mm × 10 mm), subsequently dried at 80 °C for 24 h and compressed at a pressure of 10 MPa. The specific capacitance *C* was calculated from the galvanostatic charge/discharge curves based on the following equation:

$$C = \frac{I\Delta t}{m\Delta V} \tag{1}$$

where *I* refers to the discharge current (A), *m* represents the mass of active material (g), Δt aims at the discharge time (s), and ΔV is the discharge potential range (V).

3 Results and discussion

As well known, sucrose molecule possesses abundant of –OH groups, which groups could be partially replaced by $–NH_2$ groups under hydrothermal condition by amination reaction between the sucrose and ammonia-water [17]. Figure 1 presented the FT–IR of the synthesized precursor. As shown in Fig. 1, the broad bands at 3381 and 3184 cm^{-1} correspond to the N–H stretching in $–NH_2$ or –NH groups [18] while the absorptions occurred in the 1000–1700 cm^{-1} region consistent with significant carbon/nitrogen single and double bond character. The adsorption peak of the bending vibration of $–NH_2$ is found at 1613 cm^{-1} [19, 20] while the absorption bands at 1439, 1274 and 1119 cm^{-1} is referred to aromatic C–N stretching [18], demonstrating that partial –OH groups in sucrose molecule is successfully replaced by $–NH_2$ groups.

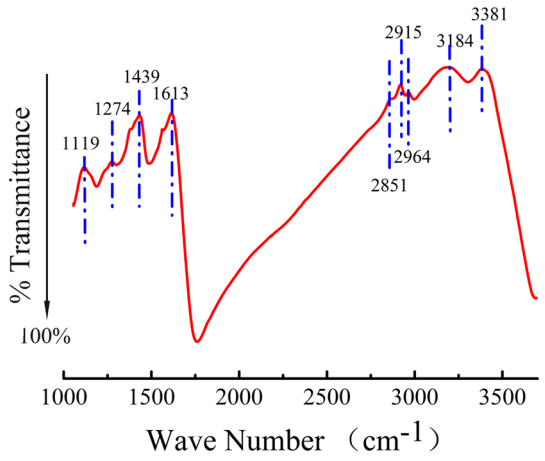

Fig. 1 FT–IR spectrum of the precursor

CHNS element analysis and XPS were employed to analyze the chemical compositions of the fabricated precursor and NDMC samples. As shown in Table 1, high N content was detected in both precursor and NDMC samples. The nitrogen content detected by CHNS element analysis and XPS is very close, illustrating a homogeneous N element distribution in the both precursor and NDMC samples. An up to 20.9 at.% N content demonstrates the nitrogen rich nature of the precursor. Beside the N element, high O content is identified in precursor (over 14.6 at.%), indicating the existence of abundant O-contained groups on surface due to the incomplete replacement of the–OH by $–NH_2$. Those O-contained groups would plays a crucial role in the future carbonization process for forming the stable carbon framework by intermolecular dehydration catalyzed by hot concentrate H_2SO_4. Although the N and O content sharply decreases during the further carbonization process, the final NDMC samples still exhibits high N heteroatoms doping level, which content is up to 10.8 at.% for the sample carbonized under 650 °C.

The chemical bond configuration of C and N elements in the fabricated NDMC materials was confirmed by high-resolution XPS spectrum. As shown in Fig. 2, the XPS spectra of the C1s orbit shows that the most dominant contribution, in all cases around 284.7 eV, comes from aromatic or other sp^2-hybridised carbon atoms bound to neighbouring carbon atoms or hydrogen [21]. Additionally slightly less pronounced peaks at around 285.4 eV and 286.6 refer to electron-poor carbon bound to nitrogen [21, 22]. For N1s, three pronounced peaks exhibits in the 392–410 eV regions. One of the peaks around 398.4 eV is commonly attributed to the pyridinic-like nitrogen species which is bound to two carbon atoms and donates one *p* electron to the aromatic π system, and another peak around 400.6 can be assigned to the pyrrolic-like nitrogen species in a five-membered carbon ring [23, 24]. The peak around 401.1 eV

Table 1 Chemical compositions of the precursor and NDMC samples

Sample ID	From element analysis			From XPS		
	at.%C	at.%N	at.%O	at.%C	at.%N	at.%O
Precursor	64.5	20.9	14.6	65.8	19.4	14.8
NDMC-650	83.4	10.8	5.8	84.0	11.6	4.4
NDMC-800	89.0	6.4	4.6	90.2	6.2	3.6
NDMC-950	92.6	4.7	2.7	91.7	5.6	2.7

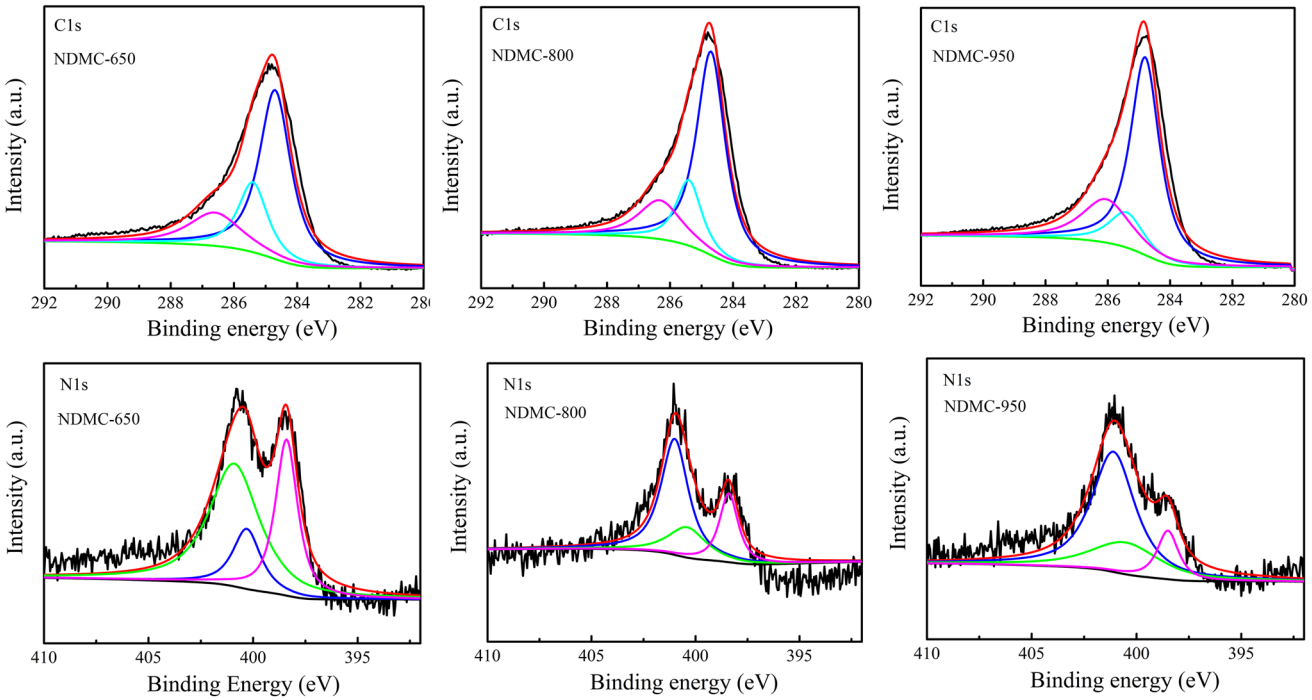

Fig. 2 XPS spectra of C1s and N1s for the NDMC samples

refers to the graphite-like nitrogen species, nitrogen atoms are incorporated into the graphene lay and replaced carbons atom within a six-membered carbon ring [25]. Overall, the XPS scans prove that the nitrogen heteroatoms are firmly incorporated into the primarily aromatic backbone of the fabricated NDMC samples.

It was reported that the doping species of nitrogen heteroatom have a crucial effect on the capacitance performance of the carbon-based supercapacitors. The pyridinic-like and pyrrolic-like nitrogen species located at the edges of the graphene layers with high physical and chemical activity due to the strong attraction for the ions, such as protons, in electrolyte induce additional pseudo-capacitance behaviors while the graphite-like nitrogen species make a contribution for the enhanced conductivity and wettability due to the *p*-doping effect and the electrically non-neutral surface induced by incorporating nitrogen heteroatoms within graphite lattice of carbon matrix [8, 15, 23, 24]. So, besides the doping level, the control for the doping species and their relative content of nitrogen heteroatoms also makes an important sense for the performance improvement of the carbon-based supercapacitors. It can be observed from Table 2, the doping species and their relative content can be adjusted by controlling carbonization temperature. Although total nitrogen content of the fabricated samples decreases from 10.8 to 4.7 at.% as carbonization temperature increases from 650 to 950 °C, the relative content of the graphite-like nitrogen species increases from 54.36 to 62.04% while that of pyrrolic-like nitrogen species increases from 14.81 to 25.62%, and the relative content of the pyridinic-like nitrogen species sharply decreases from 30.83 to 12.34%.

The fabricated NDMC materials exhibits dual mesoporous structure. As shown in Fig. 3a, the pore size distribution curves of the NDMC samples displays two sharp peaks centered around at 3.22–3.31 and 8.98–12.58 nm respectively, indicating the uniform dual mesoporous structure of the reported NDMC materials.

Table 2 Summary of XPS peak analysis on the NDMC samples

Samples	C1s (BE/eV)			N1s (BE/eV)		
	284.7 (%)	285.4 (%)	286.6 (%)	398.4 (%)	400.6 (%)	401.1 (%)
NDMC-650	58.36	22.47	19.17	30.83	14.81	54.36
NDMC-800	62.04	25.62	12.34	23.02	20.31	56.67
NDMC-950	63.50	18.27	18.23	12.34	25.62	62.04

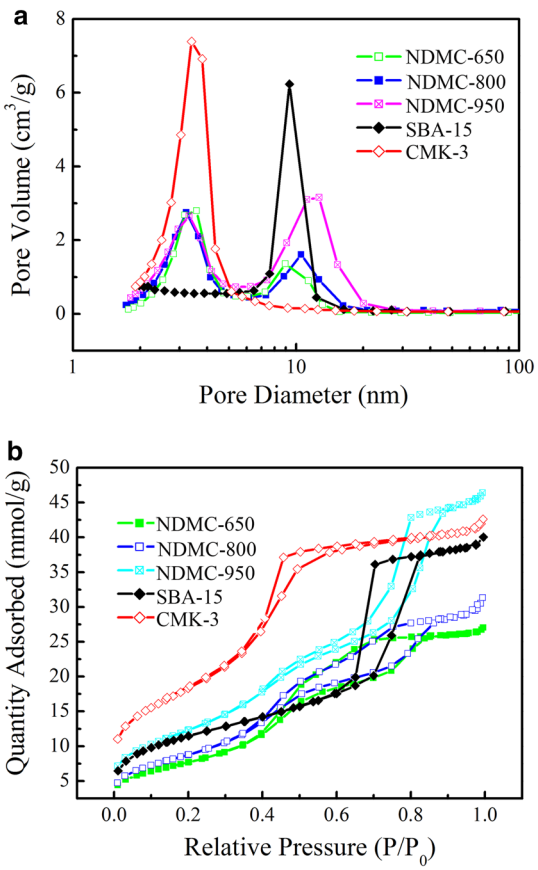

Fig. 3 Pore size distribution (**a**) and nitrogen adsorption/desorption isotherms (**b**) of the NDMC samples

Table 3 Textural parameters of the NDMC samples

Sample ID	D_p (nm)	S_{BET} (m^2 g^{-1})	V_T (cm^3 g^{-1})	V_M (cm^3 g^{-1})
SBA-15	6.58	930	1.44	1.34
CMK-3	3.43	1480	1.59	1.43
NDMC-650	3.58, 8.98	627	0.96	0.94
NDMC-800	3.22, 10.56	719	1.12	1.06
NDMC-950	3.31, 12.58	1001	1.67	1.61

D_p pore diameter, V_T total pore volume, V_M mesoporous volume

The pore size of the small mesopore is close to that of the non-doped CMK-3 which is a perfect reverse replica of the SBA-15 template, illuminates that thus small mesopore originates from the pore wall of the SBA-15 template. The large mesopore which pore size is two times higher than that of the small mesopore, and is close to the total size of the two adjacent small mesopore may be generated by the merger of adjacent small mesopore due to the collapse of the pore wall during the pyrolysis process. The increasing pore size of the large mesopore with the increasing carbonization temperature provides an indirect proof for this speculation. As shown in Fig. 3a, the pore size of the large mesopore increases from 8.98 to 12.58 nm as carbonization temperature increases from 650 to 950 °C while no apparent changes are observed for the pore size of the small mesopore. Meanwhile, the rate of the small and large mesopore can be adjusted by controlling the carbonization temperature, the small mesopore was the dominate pore structure under a relative lower carbonization temperature, but the proportion of the large mesopore continuously increases with the increasing carbonization temperature, and finally became the primary pore structure. The mesoporous nature of the fabricated materials is further proved by the nitrogen adsorption/desorption isotherms. As shown in Fig. 3b, the isotherms of the NDMC samples exhibits a typical IV adsorption behavior, and a H1 hysteresis loop at higher relative pressure could be clearly observed, typical IV adsorption isotherms with a H1 hysteresis loop is the typical characteristic of mesoporous materials. The textural parameters of the corresponding samples calculated using the data of the nitrogen adsorption/desorption isotherms and pore size distributions curves are displayed in Table 3. As shown in Table 3, the reported NDMC materials exhibits high specific surface area and large pore volume, the S_{BET} and pore volume reach up to 1001 and 1.61 cm^3 g^{-1}, respectively.

The ordered mesoporous structure of the fabricated NDMC materials is demonstrated by the SAXS patterns. As shown in Fig. 4, all samples fabricated under different carbon temperature present three well-resolved diffraction peaks, associates with 100, 110, and 200 reflections of 2D hexagonal symmetry with the space group of *p6mm* [26]. The NDMC samples exhibit similar SAXS patterns with the non-doped CMK-3 and SBA-15 template, indicates

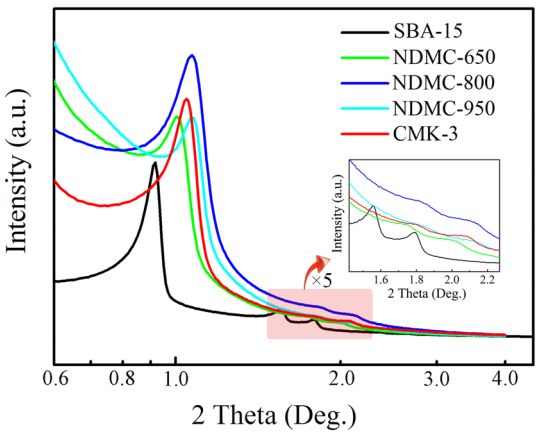

Fig. 4 SAXS patterns of the NDMC samples

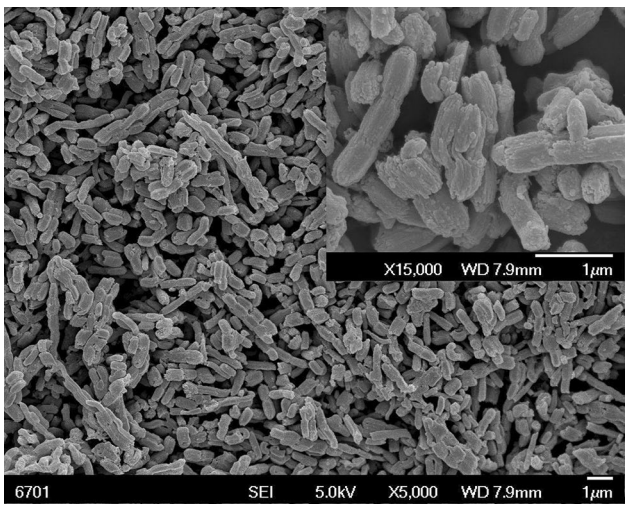

Fig. 5 Representative SEM images of the fabricated NDMC materials

that the ordered small mesoporous of the reported materials originates from the reverse replication of the SBA-15 template.

Figure 5 presents the representative SEM images of the reported NDMC materials. As shown in Fig. 5, the fabricated NDMC material exhibits a similar morphology as the template SBA-15. The typical wheat-like macrostructures of SBA-15 is successfully replicate. A long-range ordering of cylindrical channels along the 110 diffraction plane also is clearly observed. The well-ordered mesoporous structure of the fabricated NDMC materials is further proved by the TEM images. As shown in Fig. 6, the uniform stripe-like and hexagonally arranged images of the 2D hexagonal symmetry with the space group of *p6mm* can be observed clearly for all samples. Meanwhile, the merge of the adjacent mesopores also can be observed, proves that the large mesopore originates from the merge of the adjacent small mesopores.

Cyclic voltammetry (CV) was used to evaluate the capacitance behaviour of the reported NDMC materials. Figure 7 presents the CV curves of the NDMC samples at different scan rates. The reported NDMC material exhibits a composite capacitance performance of electrical double layer capacitance and pseudo-capacitance owing to the large specific surface area with highly nitrogen doped surface. In general sense, a rectangular-shape cyclic voltammograms indicates ideal electrical double layer capacitance [27, 28] while the reversible redox peaks on CV curves induced by reversible oxidation/reduction or faradaic charge transfer reactions demonstrates the existence of pseudo-capacitance [29, 30]. As shown in Fig. 7a, the non-doped CMK-3 exhibites a typical electrical double layer capacitance at a scan rate of 2 mV s^{-1}. However, at least two pairs of approximate reversible redox peaks could be observed from the CV curves of all NDMC samples, indicating the pseudo-capacitance contribution for the energy storage/releases process. Besides the redox peaks, the rectangular-like shape still can be distinguished, demonstrates that the excellent double layer capacitance still is retained after nitrogen doping. It has been reported that the quinon–hydroquinone transitions reaction responses for pseudo-capacitance of carbon materials [31, 32], but this pseudo-capacitance just exhibits an unpronounced hump on the CV curves in general sense, which contribution for total charge storage/release capability of porous carbon electrode materials can be neglected. However, as show in Fig. 7a, pronounced pseudo-capacitance can be observed after nitrogen doping, indicating that the pseudo-capacitance as well as the electrical double layer capacitance contributes to the capacitance performance of the fabricated NDMC materials. Nitrogen heteroatoms doping induces a decrease on the charge density of aromatic carbon due to the high electronegative of nitrogen atoms, which weakens the C=O and C–OH bonds on graphene lattice, and thus promotes the quinon–hydroquinone transitions reaction and then induces pronounced pseudo-capacitance [8]. With the increasing scan rates, the redox peaks gradually weakens, but the area of the rectangular-like shape proportionally increases, indicating a sequentially increasing proportion of EDLC. Even so, the redox peaks still are pronounced at a relativity high scan rate of 20 mV s^{-1}, indicating the relatively fast electron transfer rates of the redox process. The redox peaks finally completely disappears at a scan rate of 100 mV s^{-1}, illuminates the dominant contribution of electrical double layer for electric charge storage/release capability under high scan rates. Meanwhile, it should be noted that the CV curves area of the NDMC samples is

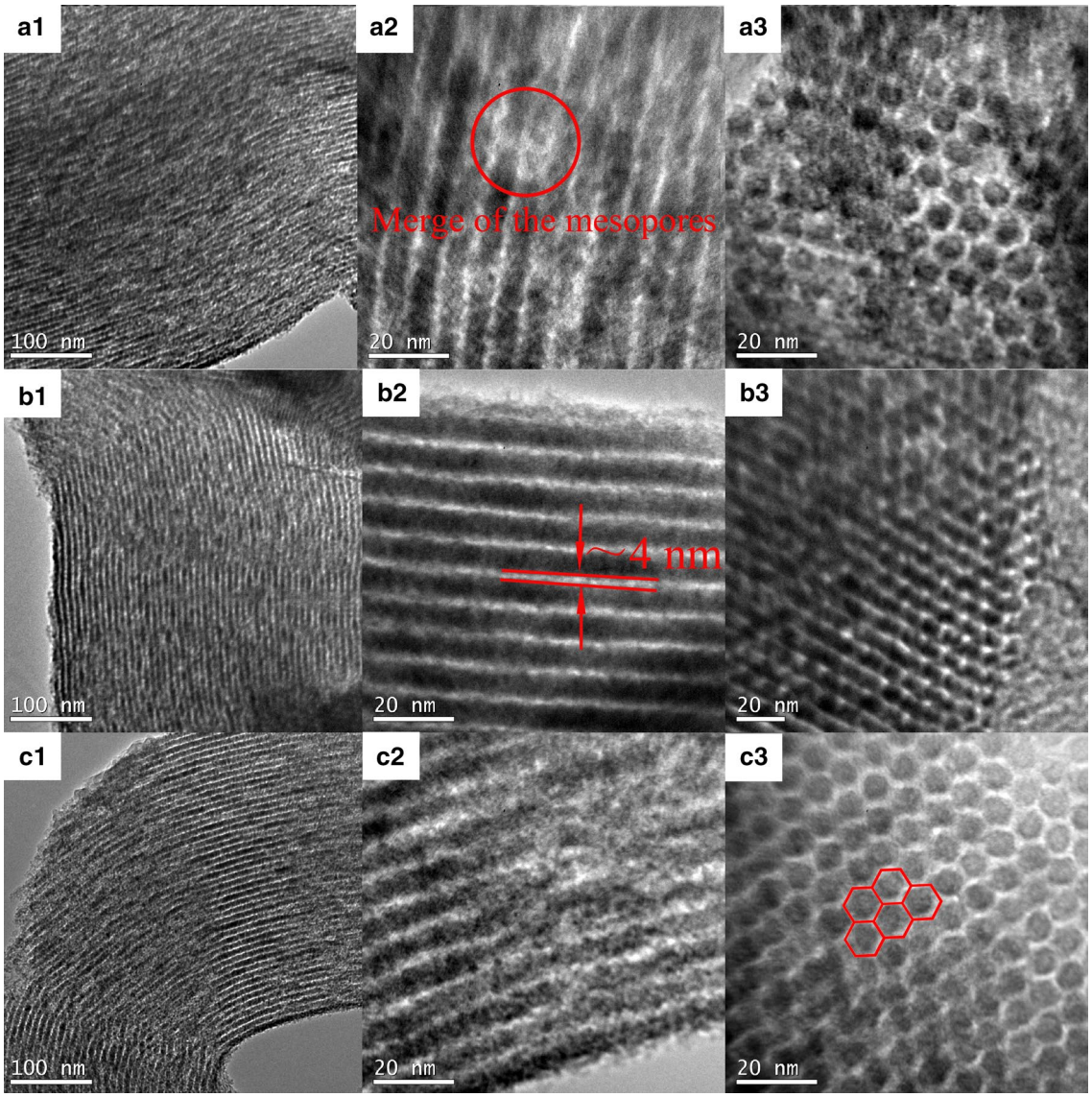

Fig. 6 Typical TEM images of the NDMC samples (**a1–a3** NDMC-650; **b1–b3** NDMC-800; **c1–c3** NDMC-950)

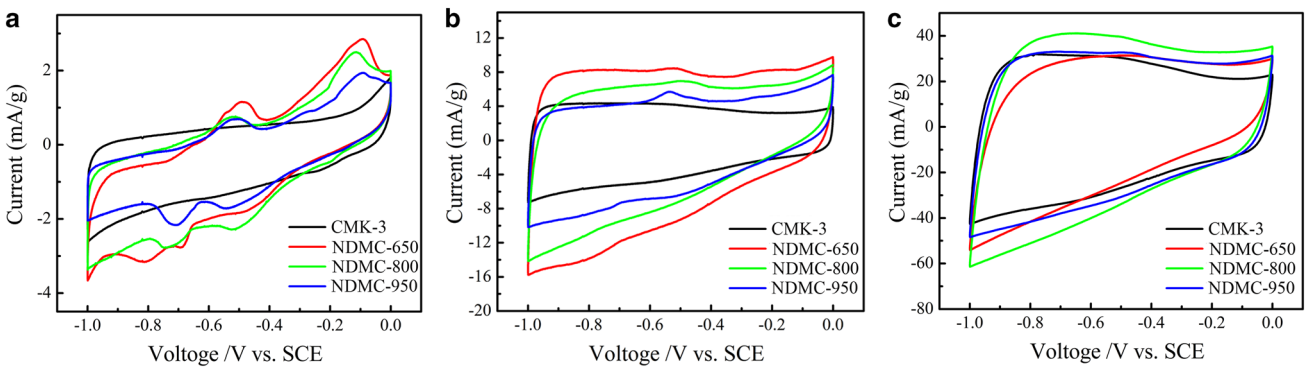

Fig. 7 CV curves of the NDMC samples at the scan rate of 2 (**a**), 20 (**b**) and 100 (**c**) mV s^{-1}

larger than that of non-doped CMK-3 even at high scan rates, illuminating the more superior supercapacitance performance of the reported materials than non-doped sample.

Figure 8 presents the charge–discharge curves of the NDMC samples. As shown in (**a**), apparent charge/discharge voltage plateaus could be observed for all NDMC samples under a current density of 0.5 A g^{-1}, illuminating the marked contribution of pseudo-capacitance for the excellent capacitance performance of the fabricated NDMC materials. The specific capacitance calculated from the discharge curves reaches up to 512, 478 and 269 F g^{-1} for NDMC-650, NDMC-850 and NDMC-950 respectively under a current density of 0.5 A g^{-1} while that of the non-doped CMK-3 only reaches 171 F g^{-1}. The specific capacitance of the NDMC-650 was three times higher than that of non-doped CMK-3, and all NDMC samples exhibits a larger specific capacitance than that of non-doped CMK-3. However, all samples present a symmetrical triangle shape which is the typical characterization of the electrical double layer capacitor as the current density increases to 5 A g^{-1} (as shown in Fig. 8b), indicates that the capacitance performance of the reported NDMC materials mainly depends on the electrical double layer capacitance rather than pseudo-capacitance under high current density. Interestingly, the decreasing nitrogen doping content causes corresponding decline of specific capacitance, illuminates the marked contribution of nitrogen heteroatoms doping for the superior capacitance performance of the reported materials. Beside the nitrogen doping, dual mesoporous structure also makes a contribution for the superior capacitance performance of the reported materials. In process of electric storage/release, the small mesopores provide the large specific surface area for forming electrical double-layer while the large mesopores provide the large pore volume for storing the electrolyte, this dual mesoporous structure effectively accelerates the diffusion rate of electrolyte in porous structure, and then enhance the capacitance performance [33]. The enhanced wettability due to nitrogen doping further accelerates this diffusion rate and improved the availability of the small mesopores [34, 35].

The presented NDMC materials exhibits reasonable cycle performance. As shown in Fig. 9, the capacitance retention rate of the sample NDMC-950 with lowest nitrogen doping content reaches 95% after 1000 cycles under a current density of 1 A g^{-1}, which value is close to that of non-doped CMK-3 (97%). The capacitance retention rate decreases with the increasing nitrogen doping content. For instance, only 76% of capacitance is retained for sample NDMC-650. Even so, all NDMC samples exhibits a significantly higher capacitance than non-doped CMK-3 after 1000 cycles, indicating the superior capacitance performance of the reported materials.

Figure 10 displays the electrochemical impedance spectroscopy (EIS) of the reported NDMC materials.The intercept of the EIS at the real impedance (Z′) axis in the high-frequency region reflects the internal resistance of the electrode, including the resistance of electrolyte, intrinsic resistance of electrode materials and their contact resistance with current collector. As shown in Fig. 10, the

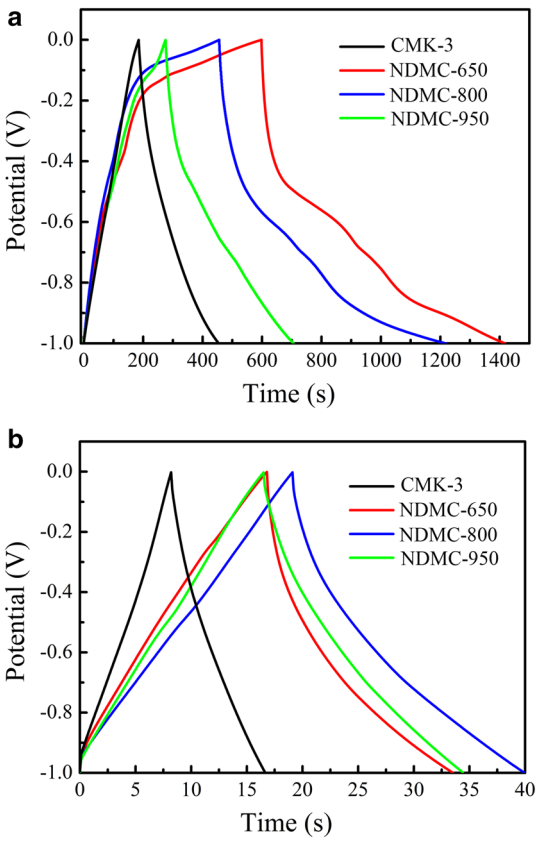

Fig. 8 Charge–discharge curves of the NDMC samples at the current density of 0.5 (**a**) and 5 (**b**) A g^{-1}

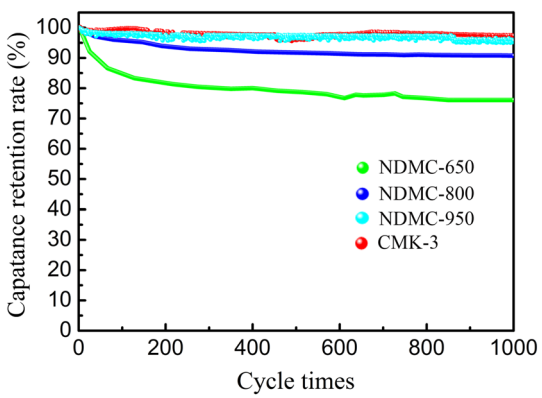

Fig. 9 Cycle performance of the NDMC samples

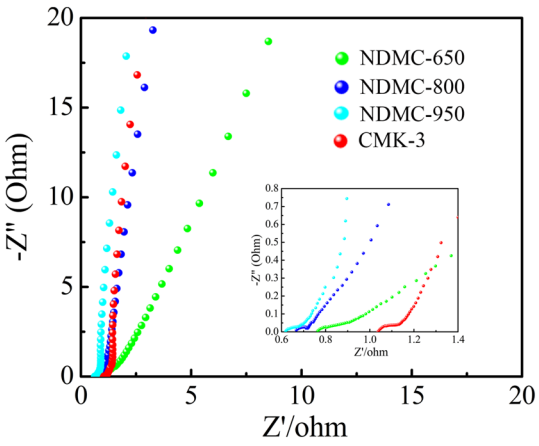

Fig. 10 Nyquist plots of the NDMC samples

internal resistance of samples NDMC-650, NDMC-800 and NDMC-950 is about 0.77, 0.68 and 0.62 Ω respectively, while that of the non-doped CMK-3 reaches about 1.11Ω, indicating the improved conductivity due to nitrogen doping. The graphite-like nitrogen species is reported to response for the improved conductivity. For graphite-like nitrogen species, the nitrogen atom is inserted into the carbon matrix and bonded to three carbon atoms, three valence electrons in graphite-like nitrogen species form σ bonds, the fourth electron fills a *p*-state, and the fifth electron forms a π*-state, giving the *p*-doping effect, which improve the conductivity of the carbon materials [36]. The decreasing internal resistance with the increasing graphite-like nitrogen species proportion proves direct evidence for this speculation.

4 Conclusion

The NDMC materials with dual mesoporous, excellent textural properties, and high nitrogen doping content fabricated using amino production of the sucrose synthesized under hydrothermal conditions as precursor exhibits superior capacitance performance. The specific capacitance of the reported materials reaches up to 512 F g^{-1}, and the capacitance retention rate after 1000 times cycles reaches 95%. The dual mesoporous structure, high specific area (up to1101 m^2 g^{-1}) as well as the additional pseudo-capacitance, enhanced wettability and conductivity induced by nitrogen doping are found to response for the superior capacitance performance of the reported materials.

Acknowledgements This work was supported by the National Natural Science Foundation of China [Grant Number 51462020, 2015]; the Key Laboratory of Eco-Environment-Related Polymer Materials of the Ministry of Education Program [Grant Number KF-13-01, 2014]; the Hongliu young teacher cultivate project of Lanzhou University of Technology [Grant Number Q201112].

References

1. J. Chmiola, G. Yushin, Y. Gogotsi, C. Portet, P. Simon, P.L. Taberna, Science **313**,1760 (2006).
2. F. Zhou, Q. Liu, D. Kang, J. Gu, W. Zhang, D. Zhang, J. Mater. Chem. A **2**, 3505 (2014)
3. Y. Zhu, S. Murali, M.D. Stoller, K.J. Ganesh, W. Cai, P.J. Ferreira, A. Pirkle, R.M. Wallace, K.a.. Cychosz, M. Thommes, D. Su, E.A. Stach, R.S. Ruoff, Science **332**, 1537 (2011)
4. Y. Zhai, Y. Dou, D. Zhao, P.F. Fulvio, R.T. Mayes, S. Dai. Adv. Mater. **23**, 4828 (2011)
5. Y. Shao, M.F. El-Kady, L.J. Wang, Q. Zhang, Y. Li, H. Wang, M.F. Mousavi, R.B. Kaner, Chem. Soc. Rev. **44**, 3639 (2015)
6. D.P. Dubal, N.R. Chodankar, Z. Caban-Huertas, F. Wolfart, M. Vidotti, R. Holze, C.D. Lokhande, P. Gomez-Romero, J. Power Sources **308**, 158 (2016)
7. X. Xu, Y. Liu, M. Wang, C. Zhu, T. Lu, R. Zhao, L. Pan, Electrochim. Acta **193**, 88 (2016)
8. D. Zhang, L. Zheng, Y. Ma, L. Lei, Q. Li, Y. Li, H. Luo, H. Feng, Y. Hao, ACS Appl. Mater. Interfaces **6**, 2657 (2014)
9. W. Sun, S.M. Lipka, C. Swartz, D. Williams, F. Yang, Carbon **103**, 181 (2016)
10. A. Ferris, S. Garbarino, D. Guay, D. Pech, Adv. Mater. **27**, 6625 (2015)
11. H. Xu, X. Hu, H. Yang, Y. Sun, C. Hu, Y. Huang, Adv. Energy Mater, 5, 1401882 (2015)
12. Z. Wang, D.O. Carlsson, P. Tammela, K. Hua, P. Zhang, L. Nyholm, M. Strømme, ACS Nano. **9**, 7563 (2015)
13. W. Jiang, D. Yu, Q. Zhang, K. Goh, L. Wei, Y. Yong, R. Jiang, J. Wei, Y. Chen, Adv. Funct. Mater. **25**, 1063 (2015)
14. H. Tang, J. Wang, H. Yin, H. Zhao, D. Wang, Z. Tang, Adv. Mater. **27**, 1117 (2015)
15. T. Lin, I.-W. Chen, F. Liu, C. Yang, H. Bi, F. Xu, F. Huang, Science **350**, 1508 (2015)
16. F. Wang, Y.-H. Xu, Z.-K. Luo, Y. Pang, Q.-X. Wu, C.-S. Liang, J. Chen, D. Liu, X.-H. Zhang, J. Power Sources **272**, (2014)
17. D. Zhang, Y. Hao, Y. Ma, H. Feng, Appl. Surf. Sci. **258**, 2510 (2012)
18. M.H. Mahaninia, P. Rahimian, T. Kaghazchi, Chin. J. Chem. Eng **23**, 50 (2015)
19. G.V.S.M. Carrera, N. Jordao, M.M. Santos, M.N. da Ponte, L.C. Branco, RSC Adv. **5**, 35564 (2015)
20. G.C. León, Y.A. Perera-Mercado, L.A. García-Cerda, J.A. Mercado-Silva, H.I. Meléndez-Ortiz, Y. Olivares-Maldonado, L. Alvarez-Contreras, Microporous Mesoporous Mater. **204**, 156 (2015)
21. R. Zhao, T. Afaneh, R. Dharmasena, J. Jasinski, G. Sumanasekera, V. Henner, Physica B **490**, 21 (2016)
22. J.P. Paraknowitsch, B. Wienert, Y. Zhang, A. Thomas, Chem. -Eur. J. **18**, 15416 (2012).
23. J. Zhao, Y. Liu, X. Quan, S. Chen, H. Zhao, H. Yu, Electrochim. Acta **204**, 169 (2016)
24. H. Liu, M. Jia, B. Cao, R. Chen, X. Lv, R. Tang, F. Wu, B. Xu, J. Power Sources **319**, 195 (2016)
25. X. Xu, Y. Li, Y. Gong, P. Zhang, H. Li, Y. Wang, J. Am. Chem. Soc. **134**, 16987 (2012)
26. D. Zhao, J. Feng, Q. Huo, N. Melosh, G.H. Fredrickson, B.F. Chmelka, G.D. Stucky, Science **279**, 548 (2010)
27. C. Vix-Guterl, S. Saadallah, K. Jurewicz, E. Frackowiak, M. Reda, J. Parmentier, J. Patarin, F. Beguin, Mater. Sci. Eng. B **108**, 148 (2004)

28. Z.-Y. Li, M.S. Akhtar, O.B. Yang, J. Alloys Compd. **653**, 212 (2015).
29. K. Zhang, L.L. Zhang, X.S. Zhao, J. Wu, Chem. Mater. **22**, 1392 (2010)
30. A. Laheäär, P. Przygocki, Q. Abbas, F. Béguin, Electrochem. Commun. **60**, 21 (2015)
31. T.J. Bandosz, J. Matos, M. Seredych, M.S.Z. Islam, R. Alfano, Appl. Catal. A- Gen. **445**, 159 (2012).
32. L. Lai, H. Yang, L. Wang, B.K. Teh, J. Zhong, H. Chou, L. Chen, W. Chen, Z. Shen, R.S. Ruoff, J. Lin, ACS Nano **6**, 5941 (2012)
33. Y. Li, Q. Liu, D. Kang, J. Gu, W. Zhang, D. Zhang, J. Mater. Chem. A **3**, 21016 (2015)
34. X. Zhao, Q. Zhang, C.-M. Chen, B. Zhang, S. Reiche, A. Wang, T. Zhang, R. Schlögl, D. Sheng, Nano. Energy **1**, 624 (2012)
35. K. Gong, F. Du, Z. Xia, M. Durstock, L. Dai, Science **323**, 760 (2009)
36. H.M. Jeong, J.W. Lee, W.H. Shin, Y.J. Choi, H.J. Shin, J.K. Kang, J.W. Choi, Nano Lett. **11**, 2472 (2011)